

# **Nonisolated switching-capacitor-integrated three-port converters with seamless PWM/PFM modulation**

Peichao Xu <sup>a b</sup>, [Huiqing Wen](#) <sup>a b</sup>, Wanjun Hao <sup>c</sup>, Yong Yang <sup>d</sup>, Jieming Ma <sup>a b</sup>, Yiwang Wang <sup>e</sup>, Jiafeng Zhou <sup>b</sup>

School of Advanced Technology, Xi'an Jiaotong-Liverpool University, Suzhou, China <sup>a</sup>

Department of Electrical Engineering and Electronics, University of Liverpool, Liverpool L69 3GJ, United Kingdom <sup>b</sup>

School of Electronic Information, Suzhou University of Science and Technology, Suzhou 215009, China <sup>c</sup>

School of Rail Transportation, Soochow University, Suzhou 215131, China <sup>d</sup>

Suzhou Vocational University, Suzhou 215104, China <sup>e</sup>

## **Abstract**

Efficiency and power density of power converters for interfacing photovoltaic panels, energy storage components such as batteries, and loads in photovoltaic (PV) systems become more and more important. Compared with individual converter design for different terminals, power-integrated multiport converters shows obvious advantages in simplifying the system structure, reducing the component count, and improving the operation reliability. Originated from the high power-density switched capacitor topology, a nonisolated switching-capacitor-integrated three-port converter (SCI-TPC) is presented to achieve single-stage direct power conversion among three ports. In order to minimize the cross-regulation effect, pulse-width-modulation (PWM) and pulse-frequency-modulation (PFM) are adopted to realize the flexible power regulation and achieve power balance among three ports. Main operation modes, power flow distribution, and power transfer characteristic are analyzed. With the seamless PWM and PFM hybrid modulation, the current stress can be reduced and the overall conversion efficiency over a full operating range can be improved. Main experimental results are provided to validate the effectiveness of the proposed concept.

- [Previous article in issue](#)
- [Next article in issue](#)

## **Keywords**

Switched capacitor converter (SCC)  
PWM/PFM modulation  
Soft-switching  
Three-port converter (TPC)

# 1. Introduction

As one typical renewable source, photovoltaic power exhibits significant fluctuations in terms of the output power since the characteristics of PV panels are highly dependent on the weather condition such as the irradiation and temperature (Subudhi and Pradhan, 2013, Koutroulis et al., 2001, Li et al., 2016). Although advanced power reserve or constant power generating techniques can be used to balance the grid changes and the uncertainty in the environmental or load conditions, energy storage components such as rechargeable batteries are still required to buffer the power fluctuations from PV panels (Crăciun et al., 2014, Sangwongwanich et al., 2017, Li et al., 2019). Thus, how to integrate the renewable energy sources, battery, and load while accommodating different operating modes and achieving high energy conversion efficiency and power density becomes a challenging design issue (Zubair et al., 2015).

In order to accommodate the charge or discharge operation of batteries, bidirectional power flow capability becomes essential for the power interface between batteries and the dc bus (Zhang et al., 2015). Fig. 1 illustrates two structures for the PV/battery hybrid power system: conventional design with individual dc/dc converters and the integrated design with multiport converters. As shown in Fig. 1(a), with the traditional structure, a unidirectional dc/dc converter and a bidirectional dc/dc converter are adopted for the PV panel and battery, respectively, which shows the limitation of high volume, large size, and low reliability (Liu et al., 2012). In order to address this issue, a novel PV system structure named as multi-port converter (MPC) has been discussed intensively, which can interface photovoltaic panels, energy storage components such as batteries, and loads in photovoltaic (PV) systems with one integrated converter. Fig. 1(b) illustrates the circuit diagram of the MPC-based architecture, which can achieve higher power density, efficiency, and system reliability compared with the conventional structure (Bhattacharjee et al., 2019, Li et al., 2019).

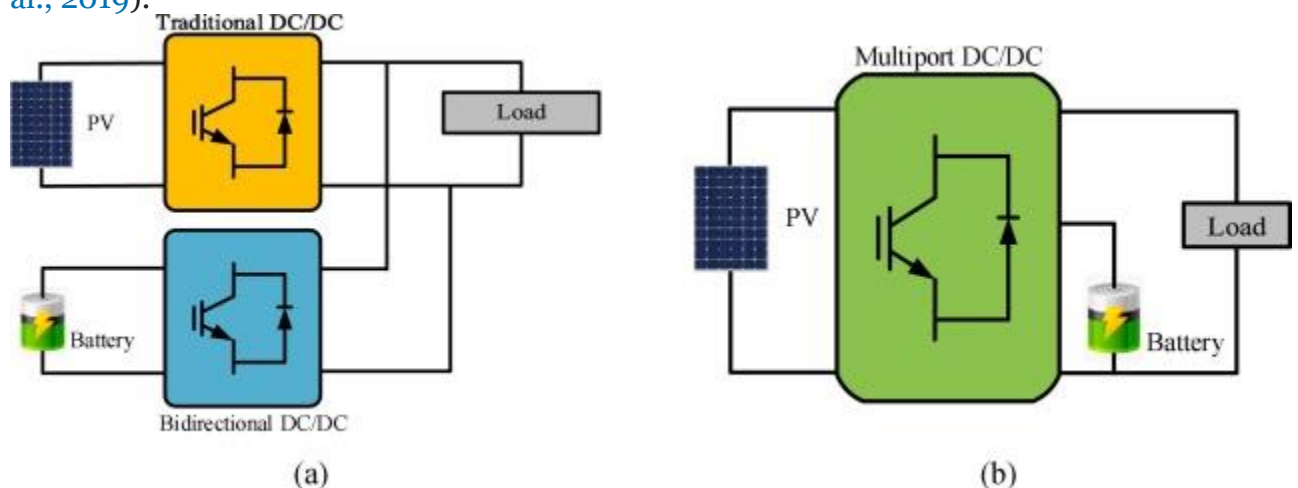


Fig. 1. Two PV system structures: (a) Individual converter topology and control; (b) integrated topology and control.

Recently, many multi-port converters (MPCs) have been discussed, which can be divided into different categories according to their power flow direction, port number, control, and isolation characteristics. Fig. 2 shows the classification of typical MPCs. For instance, taking the power flow direction as the criteria, MPCs can be divided into unidirectional and bidirectional MPCs, depending on whether the energy storage component will be involved (Hema Chander and Kumar, 2018, Majeed et al., 2019, Raghavendran et al., 2018). Taking the port number as the

criteria, MPCs can be divided into the typical three-port converters (TPCs) and MPCs with more than three ports (Prabhala et al., 2016, Zhao et al., 2015, Honarjoo et al., 2018, Mira et al., 2017, Zeng et al., 2019, Buticchi et al., 2018). TPCs can be further divided into different sub-categories, such as the dc-bus integrated converter, the photovoltaic-energy-storage integrated converter, the transformer coupled converter, and hybrid-type converters with the combination and integration of both dc bus and transformers. One typical example of MPCs with more than three ports is the quadruple active bridge (QAB) converters, which acts as the interface among the fuel cell, batteries, the super-capacitor bank, and the dc bus of the electrical power distribution system (Buticchi et al., 2018). With respect the control strategy in MPCs, PWM duty-cycle control, phase-shift control, and pulse-frequency control can be individually adopted or integrated to achieve multiple control objective simultaneously. According to the isolation characteristics, MPCs can be divided into non-isolated and isolated converters (Lavanya et al., 2016), while isolated MPCs can be further divided into complete-isolation and partial-isolation converters by using winding coupled or transformer coupled ports (Nielsen et al., 2012, Zhang et al., 2012, Zhigang and Fenlin, 2016). However, by using multi-winding transformers, the isolated MPC exhibits the limitations of large component number, large volume, high cost, and complicated hardware design and control implementation (Khosrogorji et al., 2016). Therefore, non-isolated MPCs become more popular recently due to simple structure, easy control, high power density, and reduced system cost (Ding et al., 2013, Nahavandi et al., 2015).

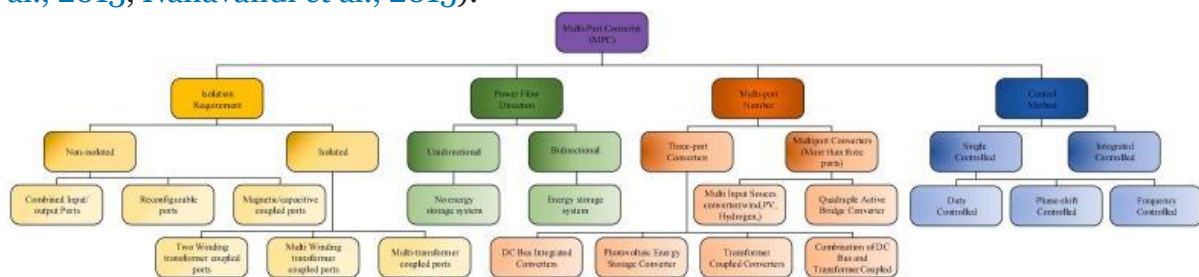


Fig. 2. Main categorization of typical MPC structure.

Among different non-isolated three-port converter (TPC) topologies, switching-capacitor (SC) based TPCs are becoming more popular recently due to their merit in achieving high power density. With the SC-based topology, the power density can be several times higher than that of the switching-inductor (SL) based topology (Sanders et al., 2013, Lei et al., 2018, Midgley and Sigger, 1974, Oota et al., 1983). Since there are no magnetic components, the voltage regulation capability of SCC is poor. To solve the shortcomings of poor voltage regulation ability, SCC is usually employing an additional inductor and complex control strategies to achieve regulation.

There are different control strategies available for TPCs: pulse-width-modulation (PWM), phase-shift control, and pulse-frequency-modulation (PFM). However, due to the power integration design, a single control cannot achieve high efficiency for a wide voltage range, decoupled regulation of the output voltage, and the flexible power regulation among three ports. To reduce the cross-regulation effect, SCI-TPC adopts the hybrid modulation of PWM and PFM to achieve flexible power regulation and power balance among three-port. Main operation modes, power flow distribution, and power transfer -characteristics are analyzed. Main experimental results are provided to validate the advantages of the proposed concept in terms of minimizing the current stress and improving the overall conversion efficiency over a full operating range.

## 2. SCI-TPC architecture and topology derivation

Fig. 3 shows the circuit diagram of the SCI-TPC, which is the integration of a switched capacitor converter (SCC), bidirectional buck-boost converter, and series resonant converter (SRC). Fig. 4 illustrated these key elements and typical waveforms in the SCI-TPC. As shown in Fig. 4(a), connected three capacitors in series, six switches are driven by complementary high and low signals (Q1, Q3, and Q5 are low-side switches, while Q2, Q4, and Q6 are high-side switches). All capacitor voltages will be automatically unified to  $V_e$  due to the circuit characteristics. Simultaneously, the nodes between the switches of the ladder-type switch capacitor converter can generate the square-wave voltage in the same phase, as shown in Fig. 4(a), which will directly act as the driving voltage of the subsequent bidirectional buck-boost converter and SRC.

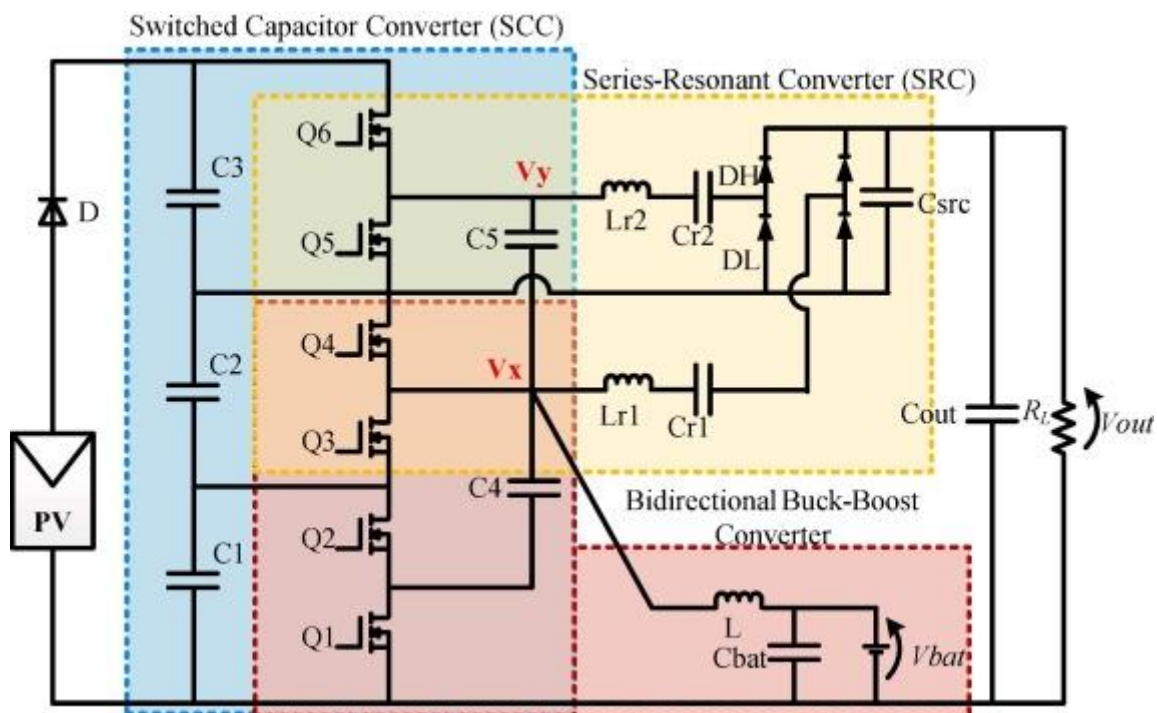


Fig. 3. Complete circuit diagram of the SCI-TPC.

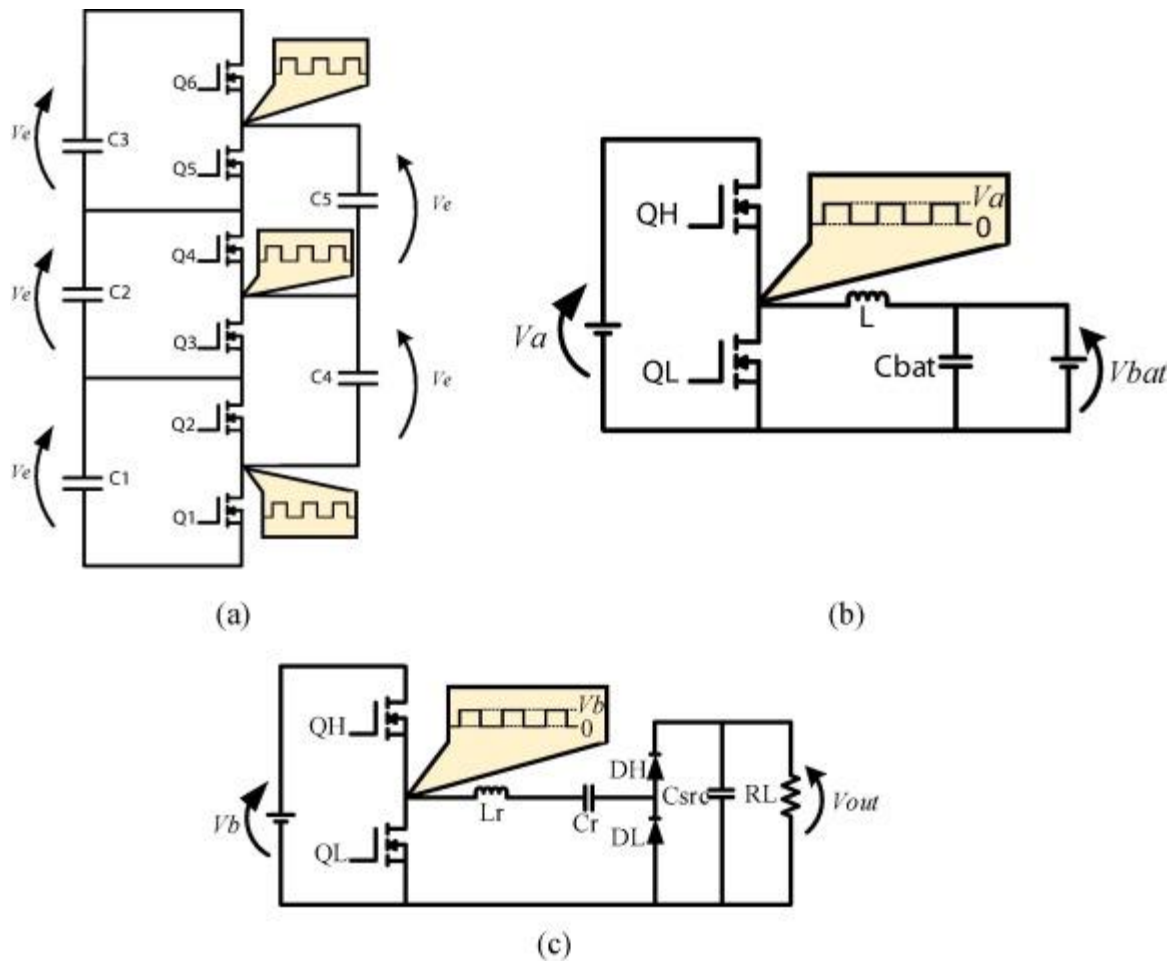


Fig. 4. Key circuit elements and typical waveforms in the SCI-TPC: (a) Switched-capacitor converter (SCC). (b) Bidirectional buck-boost converter. (c) Series resonant converter (SRC).

Considering the merits of the bidirectional buck-boost converter such as a small number of components, a simple control operation, and bidirectional power flow, it is selected in the battery port in this SCI-TPC. Fig. 4(b) shows the operation mode of the bidirectional buck-boost converter. High-side switch  $Q_H$  and low-side switch  $Q_L$  will operate alternately to produce square-wave voltages with a peak voltage of  $V_a$ . Considering the fluctuation of the voltage  $V_a$ , the battery will be charged and discharged through the regulation of the inductor current. By adjusting the square wave voltage duty cycle  $d$ , the voltage  $V_{bat}$  of the battery can be adjusted by the bidirectional buck-boost converter. Similarly, the high-side switch  $Q_H$  and low-side switch  $Q_L$  in the series resonant converter are operated alternately to generate the driving square-wave voltages with a peak voltage of  $V_b$ , as shown in Fig. 4(c). The square-wave voltage will drive the  $L.C.$  series resonator tank that is composed of  $L_r$  and  $C_r$  and produces a resonant oscillation. By controlling the switching frequency  $f_s$ , the series resonant converter will adjust the output voltage  $V_{out}$ . The series resonant converter has the features of lightweight, small size, and flexible operation.

As shown in Fig. 4, replacing  $Q_H$  and  $Q_L$  in the bidirectional buck-boost converter and SRC with  $Q_4$ ,  $Q_3$ , and  $Q_6$ ,  $Q_5$  in SCC respectively, three converters can be integrated with shared devices. Furthermore, in order to reduce the current stress and realize soft switching operation of the switch meanwhile reducing the RMS current of each resonant tank, two resonant tanks are adopted and connected to two different

switching nodes,  $V_x$  and  $V_y$ , respectively in the integrated converter. The square-wave voltages produced by  $V_x$  and  $V_y$  switch nodes will drive and resonant tanks, respectively.  $V_x$  is also responsible for the drive of inductance  $L$  in the bidirectional buck-boost converter. Due to the high integration brought by switch sharing and the circuit simplification, the SCI-TPC shows the merit of high power density, which is suitable for the applications that require simplified systems and miniaturization such as satellite power systems.

### 3. Operation mode and power characterization of SCI-TPC architecture

#### 3.1. Operation modes

As mentioned above, the SCI-TPC is controlled by two freedoms, the duty cycle  $d$  and switching frequency  $f_s$ , by using the hybrid PWM-PFM modulation. Their objectives are to regulate the output voltage and manage the battery charge and discharge operation of batteries. According to the change of environmental conditions, the converter can be divided into three working modes, as shown in Fig. 5. A simple equation can express the power balance:  $P_{in} = P_{out} + P_{bat}$

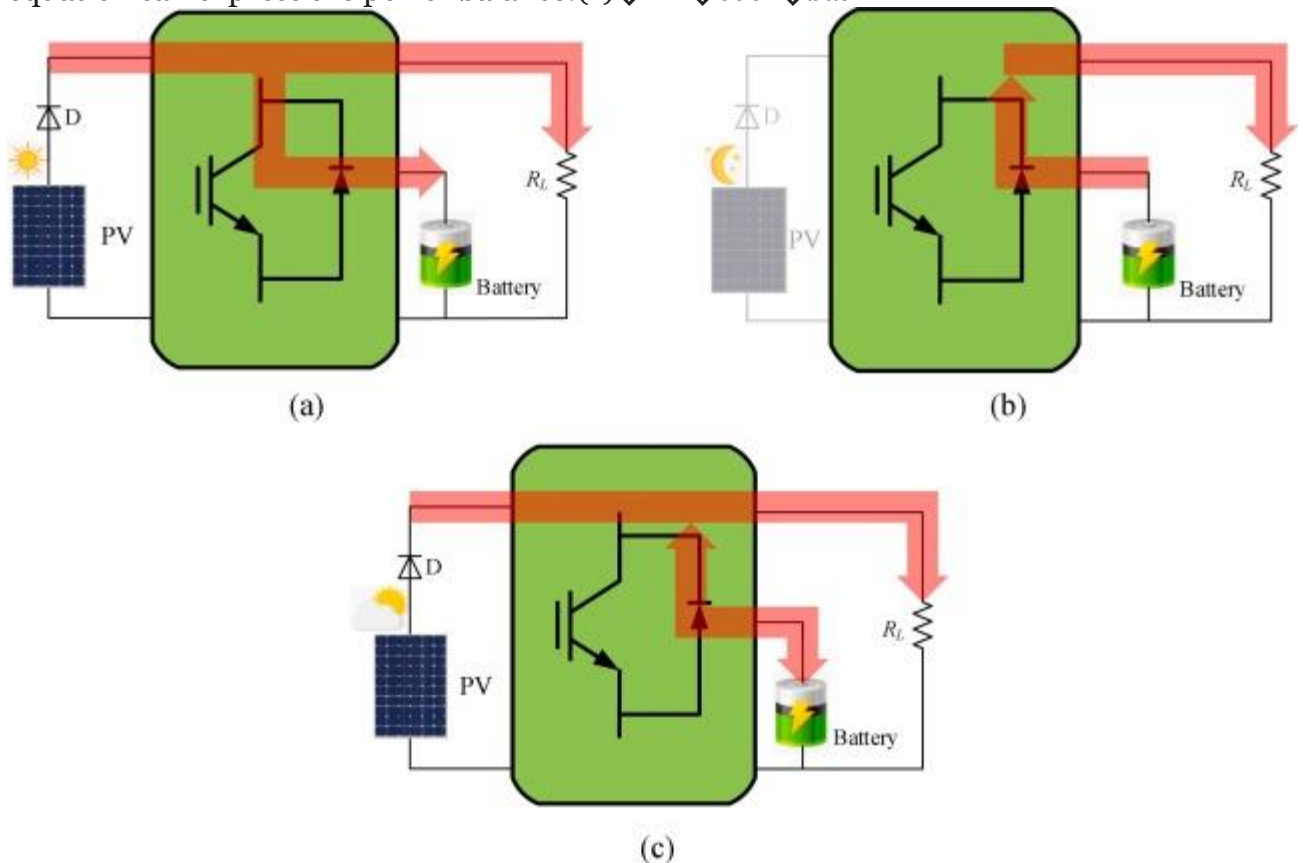


Fig. 5. Power flow distribution for different modes: (a) Battery charging mode. (b) Battery discharging mode. (c) Maximum power point tracking mode (MPPT). where  $P_{in}$ ,  $P_{out}$ , and  $P_{bat}$  represent the input power, output power, and battery charging power, respectively.

Under the power balance constraint of (1), the SCI-TPC operation can be divided into battery charging mode, battery discharging mode, and maximum power point

tracking mode (MPPT) According to the power balance among various ports. Fig. 5 illustrated the power flow distribution for three modes and each mode will be described as follows:

**Battery charging mod:** as shown in Fig. 5(a), the power generated by photovoltaic panels can fully ensure the demanded output power, and the residual power can be used to charge the battery so that the output voltage is well controlled. In this mode,  $V_{bat}$  and  $V_{out}$  are regulated by two control freedoms,  $d$  and  $f_s$ , respectively.

**Battery discharging mode:** as shown in Fig. 5(b), photovoltaic panels do not perform power generation operations especially during the night, in which case the output power of the load is entirely alone supplies by the battery's discharge power, namely  $P_{out} = -P_{bat}$ . In this mode,  $V_{out}$  is regulated by two control freedoms,  $d$  and  $f_s$ .

**MPPT mode:** as shown in Fig. 5(c), when the maximum power generated by photovoltaic panels is controlled by MPPT to be greater than the output power or less than the output power, the battery shall be responsible for buffering the surplus or shortage of power from photovoltaic panels in order to ensure that the expected output power can be reached. In this mode,  $P_{in}$  is regulated by switching duty cycle  $d$  due to MPPT controlled operation, and meanwhile,  $V_{out}$  is regulated by  $f_s$ . The charge and discharge of the battery are based on a seamless switch among three ports while maintaining good power balance.

## 3.2. Mode operation waveforms

### 3.2.1. Battery charging mode

In this mode, both the load power and the charging power to batteries are supplied by the photovoltaic panel. Fig. 6 shows key operation waveforms of the SCI-TPC during the battery charging mode. The high side switches  $Q_2$ ,  $Q_4$ ,  $Q_6$ , and the low side switches  $Q_1$ ,  $Q_3$ ,  $Q_5$  are driven in complementary mode. The voltage across the capacitor 1-3 in SCC for the steady state is set as  $in/3$ . For the resonant network, the

resonant frequency  $f_r$  can be expressed by:(2)

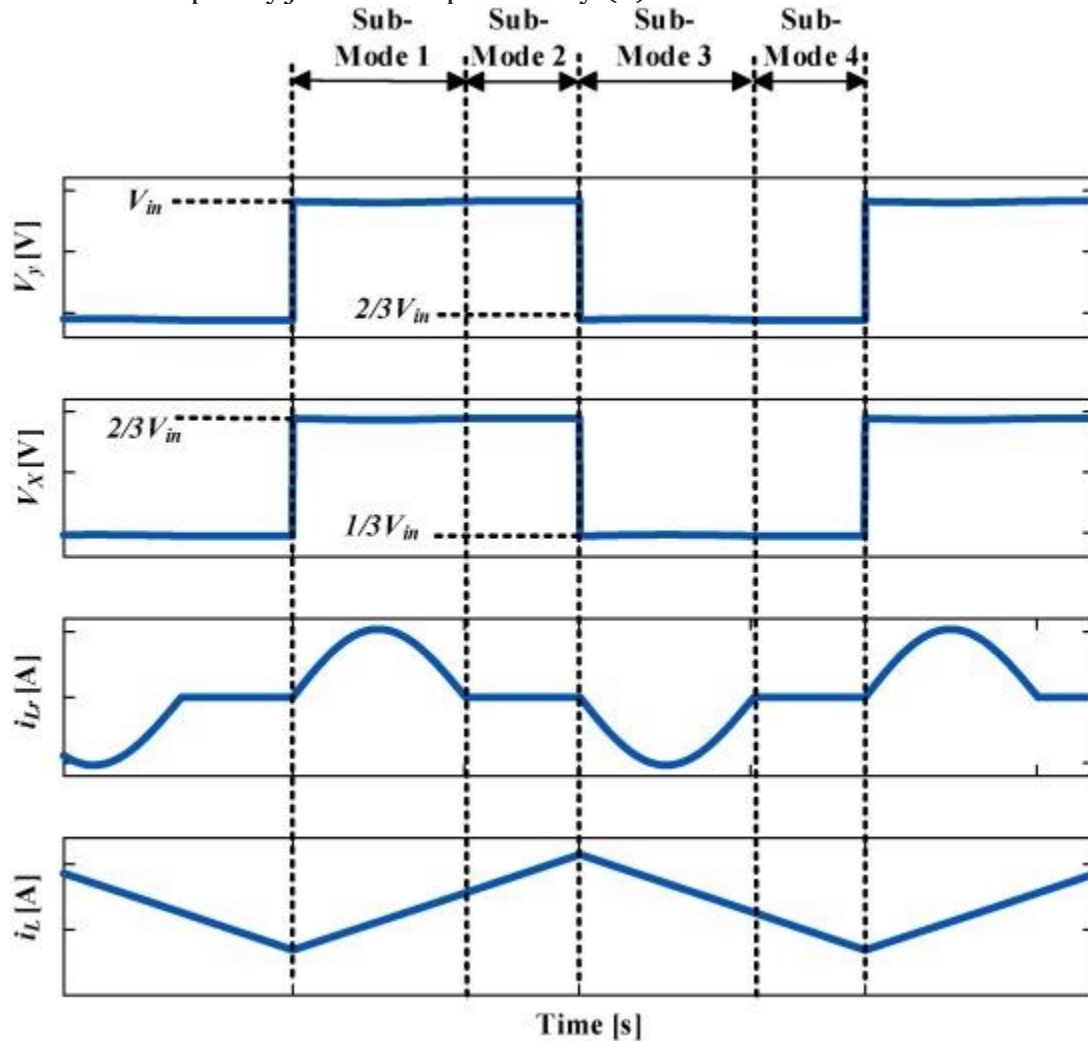
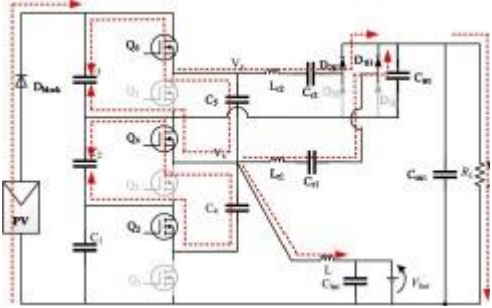
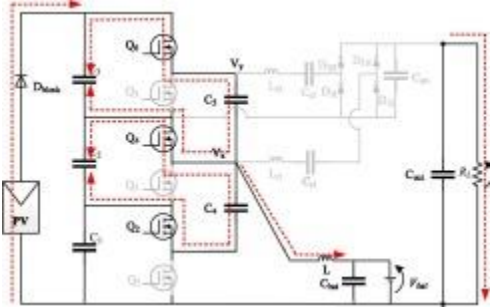
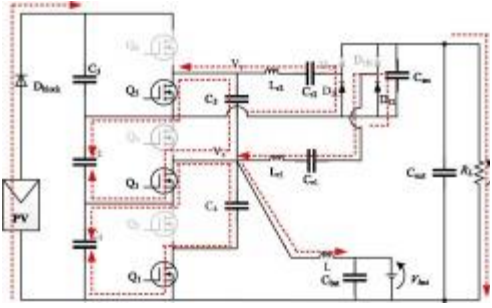
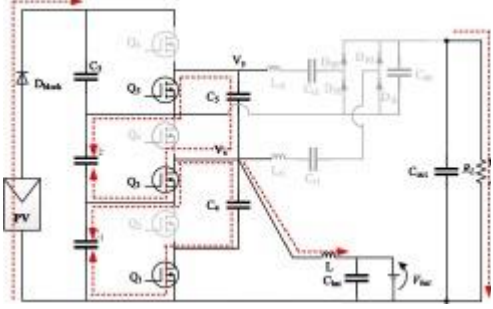


Fig. 6. Key operation waveforms of the SCI-TPC during the battery charging mode, where  $L_r$  and  $C_r$  represent the equivalent inductance and capacitor of the resonant tank, consisting of  $L_{r1}$ ,  $L_{r2}$ ,  $C_{r1}$ , and  $C_{r2}$ .

[Table 1](#) show the detailed current flow of the SCI-TPC during the battery charging mode. Due to the characteristics of SCC, the voltage across the capacitor will be automatically unified to  $V_{in}/3$ . Besides, the inductor  $L$  of the bidirectional buck-boost converter and the resonant tank of SRC will be driven by the square-wave voltage of  $V_x$  and  $V_y$  switch nodes, respectively. In order to clearly show the operation of the SCI-TPC during this mode, four sub-modes are divided and their detailed operations are analyzed in [Table 1](#):



Table 1. The Detailed Operations Of Sci-Tpc During The Battery Charging Mode.

Sub-Mode	Current Flow	Turned-On Switches	Voltages $V_x$ and $V_y$	Current $i_L$	Current $i_L$
Sub-Mode 1		Q2, Q4, Q6	High level	Increase linearly	Positive
Sub-Mode 2		Q2, Q4, Q6	High level	Increase linearly	Zero
Sub-Mode 3		Q1, Q3, Q5	Low level	Decrease linearly	Negative
Sub-Mode 4		Q1, Q3, Q5	Low level	Decrease linearly	Zero

### 3.2.2. Battery discharging mode

In this mode, the photovoltaic panels are not generating power especially during the night. The load power is provided entirely by the discharge power of batteries. Fig. 7 shows key operation waveforms of the SCI-TPC during the battery discharging mode. In order to clearly show the operation of the SCI-TPC during this mode, four sub-modes are divided. The detailed current flow of the SCI-TPC for four sub-modes and their detailed operations are analyzed in Table 2:

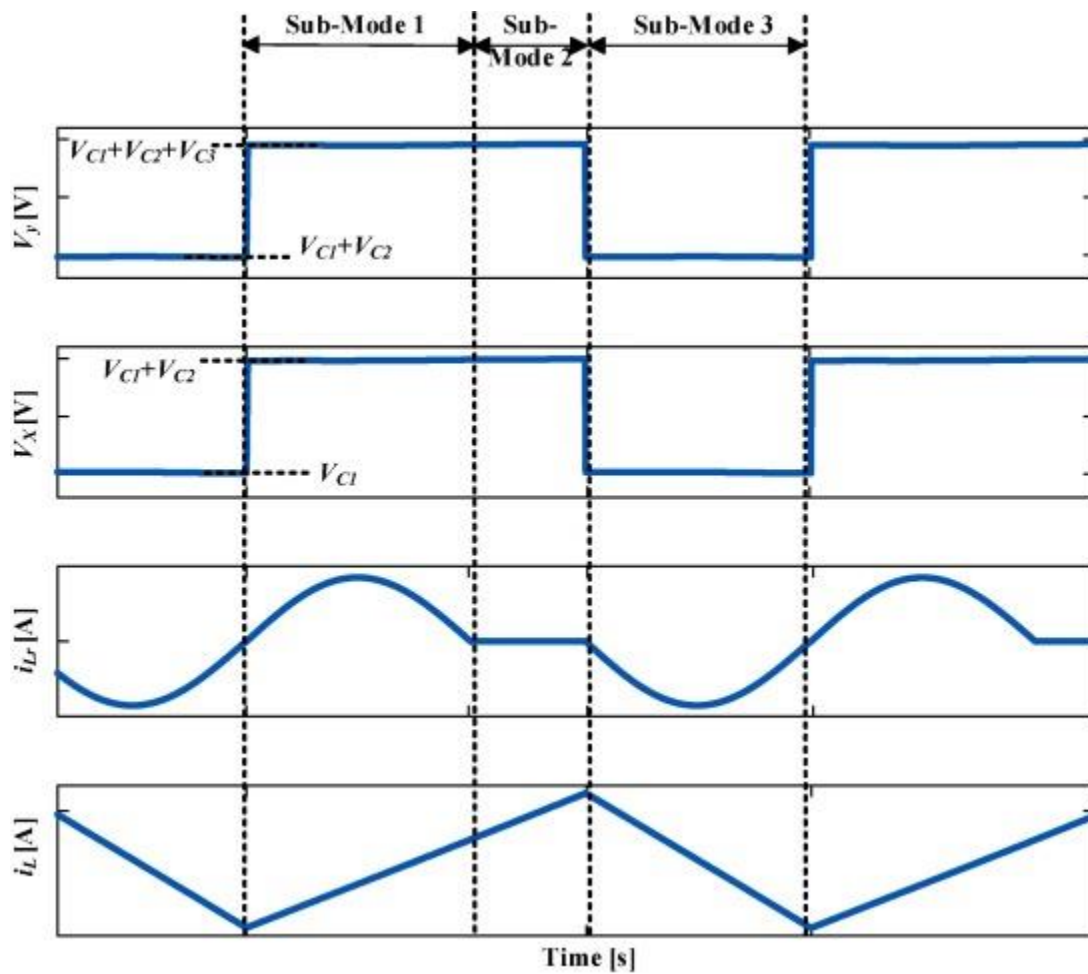
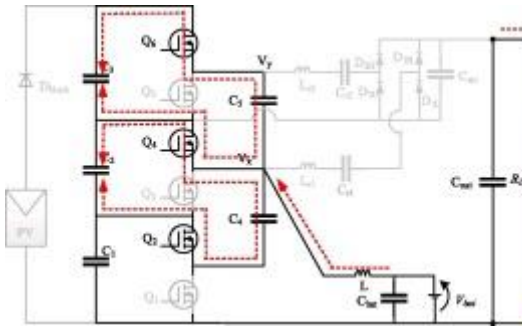
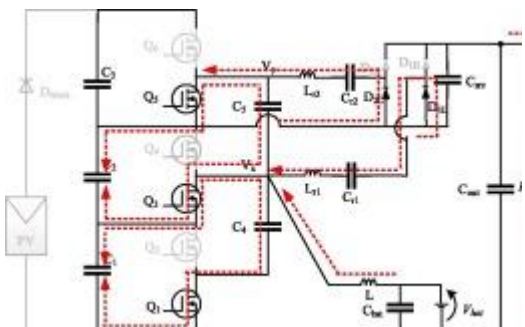


Fig. 7. Key operation waveforms of the SCI-TPC during the battery discharging mode.  
 Table 2. The Detailed Operations Of Sci-Tpc During The Battery Discharging Mode.

Sub-Mode	Current Flow	Turned-On Switches	Voltages $V_x$ and $V_y$	Current $i_L$	Current $i_t$
Sub-Mode 1		Q2, Q4, Q6	High level	Increase linearly	Positive

Sub-Mode	Current Flow	Turned-On Switches	Voltages $V_x$ and $V_y$	Current $i_L$	Current $i_r$
Sub-Mode 2		Q2, Q4, Q6	High level	Increase linearly	Zero
Sub-Mode 3		Q1, Q3, Q5	Low level	Decrease linearly	Negative linearly

### 3.3. Operation criterion

During the battery charging mode, considering that the SCI-TPC is composed of a bidirectional buck-boost converter and SRC, the main concern is the couple effect since the control variable  $d$  in PWM may affect the variable  $f_s$  in PFM. As illustrated in Fig. 6 and Table 1, SRC will not be involved in Sub-Mode 2 and Sub-Mode 4, indicating that SRC is not affected by the duty cycle under certain conditions. In order to implement Sub-modes 2 and 4 throughout the operating period, half of the resonance period ( $1/2$ ) must be shorter than and  $1-$ . Based on the limitation, the relationship that the  $f_s$ ,  $f_r$ , and  $d$  need to meet can be expressed by:

$$(3) \frac{1}{2} \leq \frac{1}{2} \leq 1 - (4) \frac{2}{2} \leq 1 - 2$$

During the battery discharging mode, the battery energy will provide power to the load through the bidirectional buck-boost converter and SRC. Therefore,  $V_{out}$  will be regulated by both  $d$  and  $f_s$ . For the convenience of research and discussion, the ratio of  $f_r$  to  $f_s$  is defined as  $F$ , the expression is given by:

$$(5) = /$$

Then, the function of  $F$  with  $d$  can be obtained and illustrated in Fig. 8. It can be clearly seen that  $F$  reaches its peak when  $=0.5$  and decreases linearly as  $d$  moves away from 0.5.

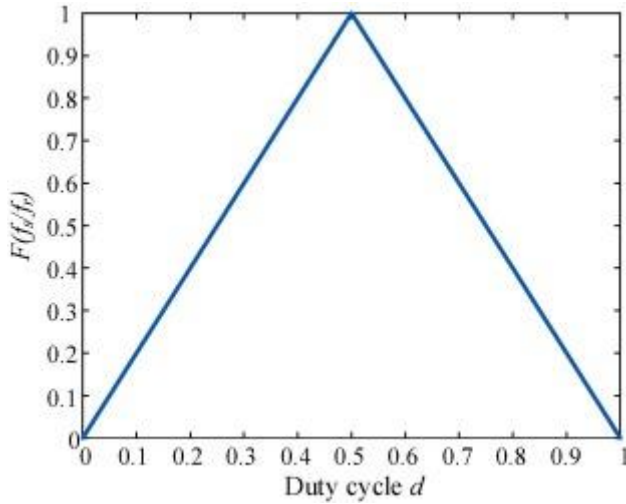


Fig. 8.  $F$  as a function of  $d$  in battery charging mode.

### 3.4. Battery voltage conversion ratio

The SCI-TPC is only controlled by PWM to realize the battery voltage regulation. According to Fig. 6 and Fig. 7, it is evident that the node voltage  $V_x$  fluctuates between  $2/3V_m$  and  $1/3V_m$ . According to the voltage-second balance on the inductance  $L$ , the battery voltage  $V_{bat}$  and the battery voltage conversion ratio  $M_{bat}$  can be derived as:

### 3.5. Output voltage conversion ratio

During the battery charging mode, the SCI-TPC uses PFM to control the switching frequency  $f_s$  in order to adjust the output voltage in SRC. Due to the constant (4),  $f_s$  must be set less than or equal to  $f_r$  to ensure the regular operation of resonant converters. As shown in Fig. 6, considering that two resonant tanks have the same peak-to-peak voltage in/3, therefore, a simplified analysis on one resonant tank is selected by neglecting Sub-modes 2 and 4. Fig. 9 shows the simplified circuit and typical waveforms of SRC in the SCI-TPC.

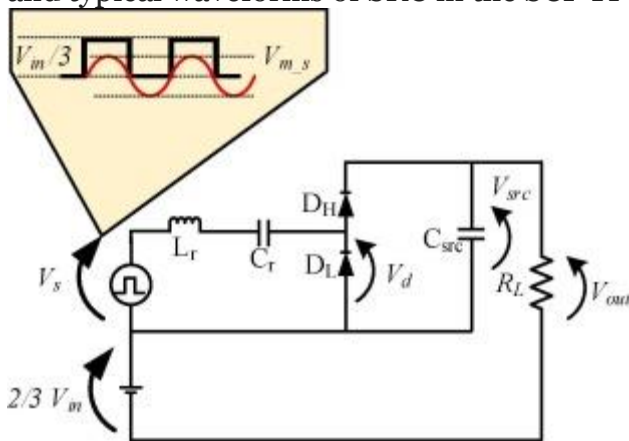


Fig. 9. Simplified circuit and typical waveforms of SRC in the SCI-TPC.

According to the fundamental harmonic approximation, the square-wave voltage on  $V_x$  and  $V_y$ , and the square-wave voltage on the rectifier bridge can be transformed into sinusoidal waveform  $V_s$  and  $V_d$  and their amplitudes can be obtained as:(8) where  $V_f$  represents the forward voltage drop of the diode,  $V_{src}$  is the voltage of the capacitor  $C_{src}$ .

Then, considering the total resistance of the resonant tank  $R_{res}$ , the current amplitude of  $i_{Lr}$ ,  $I_m$ , can be expressed as:(9)

Meanwhile, the charge quantity of  $C_r$  in Sub-mode 1 and Sub-mode 3,  $Q_{Cr}$ , can be expressed as:(10)

Since the SCI-TPC has two resonant tanks, the average output current  $I_{out}$  can be expressed by:(11)

Combining (9), (11), the expression for the output voltage can be derived as:(12)

From the equation (12), it is interesting noted that the output voltage is only related to the ratio of resonant frequency  $f_r$  to switching frequency  $f_s$  and is independent of the switch duty cycle  $d$ . The equation indicates that the SCI-TPC can adopt any switching duty cycle once the switching duty cycle  $d$  satisfies the constraint (4).

Define the ratio of  $R_{res}$  to  $R_L$  as  $R$ , the expression is given by:(13)

Combining (5), (12), the output voltage gain  $M$  can be obtained as:(14)

Then, the theoretical gain can be calculated and illustrated in Fig. 10.

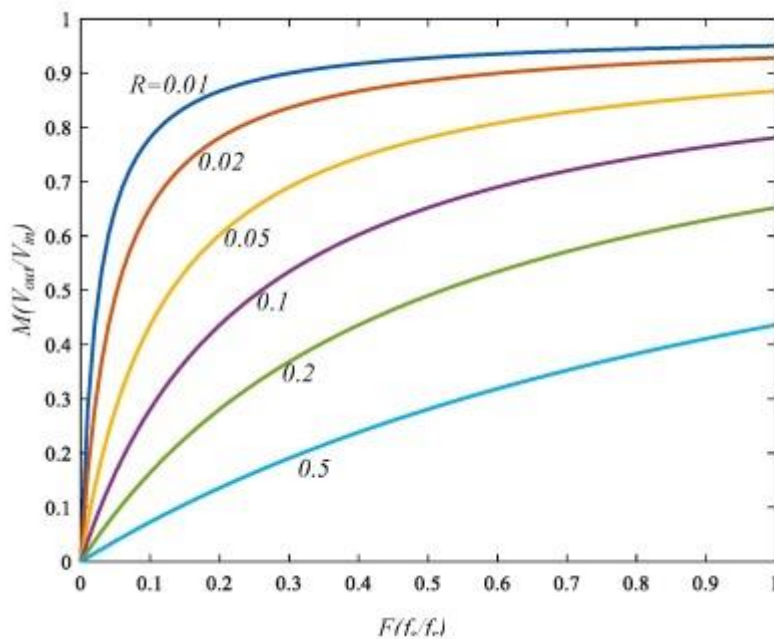


Fig. 10. Theoretical input-to-output voltage gain with respect to F.

## 4. Hybrid PWM/PFM control for SCI-TPC architectures

### 4.1. Inductor rms current oriented optimization

In order to minimize  $I_{Lr\_RMS}$  and maximize power conversion efficiency, the two control freedoms,  $d$  and  $f_s$  must be optimized.  $I_{Lr\_RMS}$  during the battery discharging mode can be expressed as:(15) Then,(16) The expression for the optimal  $d$  can be derived as:(19)

Thus, the relationship between  $I_{Lr\_RMS}$  and  $f_s$  can be obtained for a given  $P_{out}$ , as shown in Fig. 11:

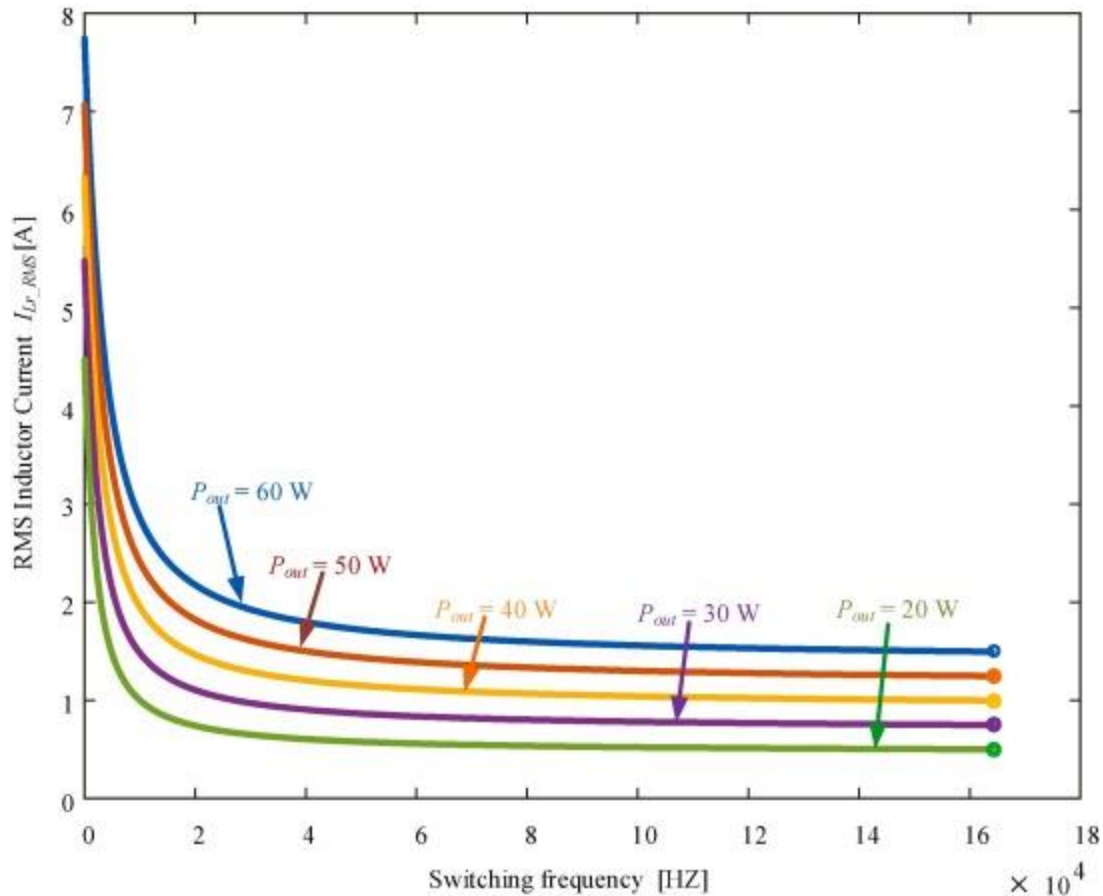


Fig. 11. Theoretical relationship between  $I_{Lr\_RMS}$  and  $f_s$ .

It can be seen from Fig. 11 that  $I_{Lr\_RMS}$  will decrease with the switching frequency  $f_s$ . However, in order to ensure that the normal operation of the resonant tank, the switching frequency cannot be greater than the resonant frequency. In other words, the switching frequency  $f_s$  can only reach the resonant frequency  $f_r$  at most. It can be calculated that when  $0.5$  and  $I_{Lr\_RMS}$  is minimum. At this point, the inactive periods in SRC are completely eliminated to achieve the minimum  $I_{Lr\_RMS}$ . It can be seen that due to the elimination of inactive period, the  $I_{Lr\_RMS}$  current in SRC decreases, which means the joule loss in SRC decreases, so that the efficiency of this converter will be improved. With the exception of the special cases where  $=0.5$  and  $=$  where  $\neq 0.5$  and making or  $1/$ -equal to  $1/2$ , one inactive period can be eliminated to reduce  $I_{Lr\_RMS}$  and Joule loss in the SRC.

In this paper, in order to reduce the current stress and improve the overall conversion efficiency over a full operating range, a seamless PWM and PFM hybrid modulation is adopted. Specifically, in the selection of key variables  $f_s$ ,  $f_r$ , and  $d$ , the following relationship is adopted:(20)

Thus, the relationship between  $d$  and  $f_s$  must satisfy the formula to ensure the optimal operation of the resonant tank and achieve the lowest  $I_{Lr\_RMS}$ .

#### 4.2. System control diagram

Fig. 12 shows the system control diagram of the hybrid PWM/PFM control, where  $V_{out}$  and  $V_{bat}$  are adjusted by PI Controllers. In all operating modes,  $V_{out}$  is only regulated by the switching frequency  $f_s$ , because  $V_{out}$  must pass through SRC. Once the switching frequency  $f_s$  is determined,  $V_{bat}$  or  $P_{in}$  can be adjusted by the duty cycle of the active switches,  $d$ . Specifically, in the battery charging mode, a PI Controller is

adopted to directly regulate  $V_{bat}$  by adjusting the variable  $d$ . However, in the battery discharging mode, considering the coupling relationship between  $f_s$  and  $d$ , the hybrid PWM/PFM algorithm will adopt the equation to determine the variable  $d$  from the  $f_s$ , which is determined by the PI control of the output voltage,  $V_{out}$ . In MPPT mode, the variable  $d$  is obtained by implementation of the MPPT algorithm according to the measured  $V_{in}$  and  $I_{in}$ . Finally, the maximum power yield can be ensured for PV panels under various operating conditions. In this paper, a classical perturbation and observation (P&O) MPPT algorithm is implemented to achieve maximum power point of photovoltaic panels (Lavanya et al., 2016). Fig. 13 shows the detailed flowchart of the P&O MPPT algorithm.

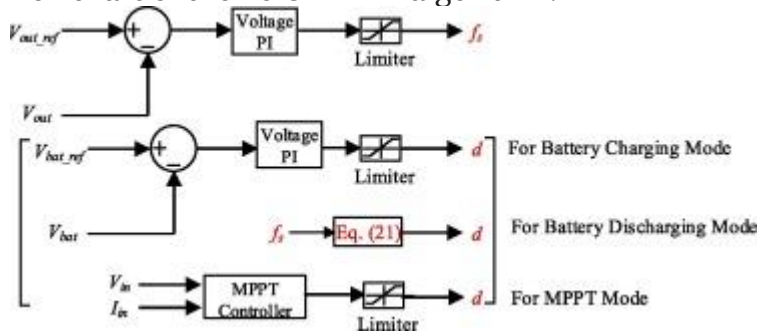


Fig. 12. System control diagram of the hybrid PWM/PFM.

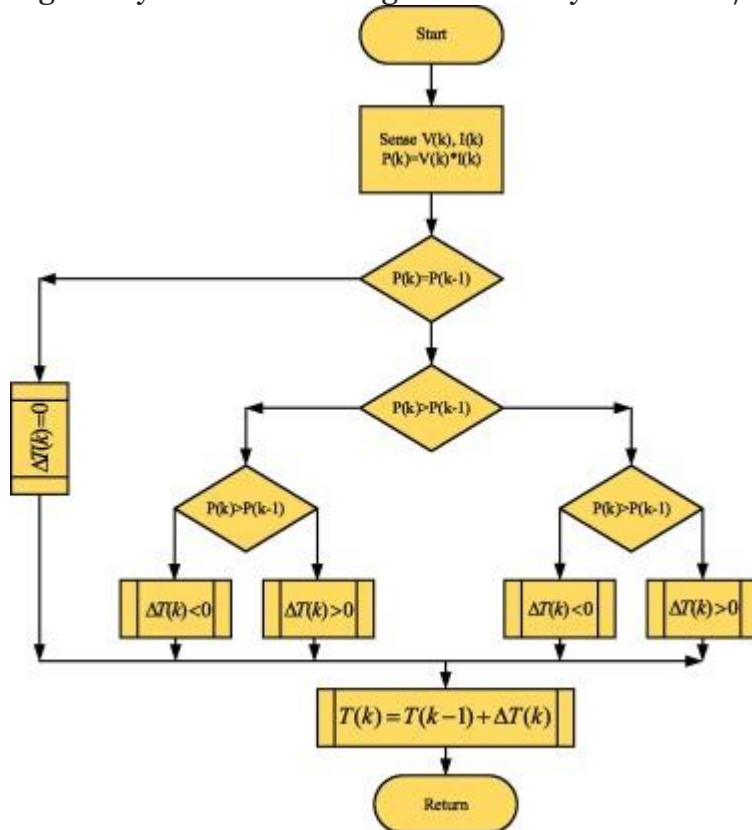


Fig. 13. Flowchart of the MPPT algorithm.

## 5. Simulation evaluation

In this section, main modes of the SCI-TPC, including the battery charging, battery discharging, and MPPT mode, are simulated by establishing simulation models in MATLAB. All simulation conditions are shown in Table 3, where the current source

and voltage source are regulated as the output and input ports, respectively. For example, in the battery charging mode, the output ports include both the battery and load, which is emulated by the current source, and the PV panel is adopted as the input port, which is emulated by a voltage source. Table 3 listed the simulated results of main circuit parameters during different modes.

Table 3. Simulated Results of Key Circuit Parameters During Different Modes.

Parameter	Battery Charging	Battery Discharging	MPPT
$V_{in}$ [V]	45	–	45
$I_{in}$ [A]	–	–	0.89
$I_{out}$ [A]	1.395	1.395	1.395
$V_{out}$ [V]	43	43	43
$V_{bat}$ [V]	22	22	22
$I_{bat}$ [A]	0.91	–	–
$d$	0.5	0.6	0.5
$F$	0.49	0.8	0.49

Simulated results of the current stress for all active power devices are listed in Table 4, which indicates the maximum current of these switches is different for different operation modes and the highest current stress of each switch is labelled with yellow. Since the input port in the battery charging mode will provide the power to the battery port and the load port, all input currents reach the highest, such as high current stress in 4-6 for this mode. For the battery discharging mode, the current is mainly concentrated in 1-3 since the battery will provide power to the output port through discharging on low-side devices.

Table 4. Simulated Current Stress of Main Power Devices.

Switch	Battery Charging [A]	Battery Discharging [A]	MPPT [A]
$Q_1$	–5.5	14.1	3.7
$Q_2$	–6.1	12.2	2.8
$Q_3$	–6.3	9.1	4.3
$Q_4$	12.2	–9.5	5.4
$Q_5$	18.9	–15.3	15.0
$Q_6$	14.4	2.0	7.6

The key waveform and current flow in the MPPT mode should be the same as those in the battery charging mode. In addition to regulate  $V_{out}$  through the PFM, during the MPPT mode, the PWM control will be adopted to reach the maximum power point of input power  $P_{in}$  of photovoltaic panels through the regulation of the switch duty cycle  $d$ . Depending on the power balance between three ports, the battery will buffer the different power through the charging or discharging operation. The seamless power flow switching operation among three ports during the MPPT mode is illustrated in Fig. 14.



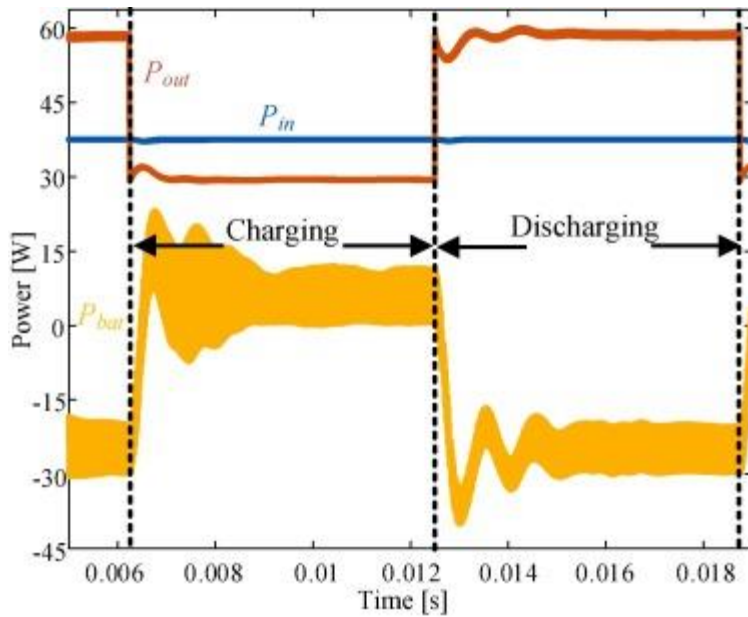


Fig. 14. Simulated output power results during different modes.

## 6. Experimental results

### 6.1. Prototype

In order to verify the effectiveness of the hybrid PWM/PFM, an 80-W prototype of the SCI-TPC was built, as shown in Fig. 15. Main parameters for the built prototype include , and the resonant frequency  $f_r$  was 164 kHz. Considering the current stress difference, a dual MOSFET IRF7905 with low on-resistance  $R_{ds(on)}$ , 21.8 and 17.1m $\Omega$  for the upper and lower device respectively, was used for the prototype. The photocoupler TLP250 was used in the gate driving circuit to improve the driving reliability. In the practical design, 188  $\mu F$  ceramic capacitors were used for, and 140  $\mu F$ , 70  $\mu F$  and 110  $\mu F$  ceramic capacitors were adopted for  $C_{src}$ ,  $C_{out}$  and  $C_{bat}$ , respectively. For the resonant network 0.47  $\mu H$  inductor and 2  $\mu F$  capacitor were used and connected in series. A schottky diode  $D_H$  and  $D_L$  with the forward voltage =0.39 and a 33  $\mu H$  inductor  $L$  (9 $\times$ 95) with low on-resistance 30 m $\Omega$  at 100 kHz were adopted for the 80 W prototype. All components list is shown in Table 5.

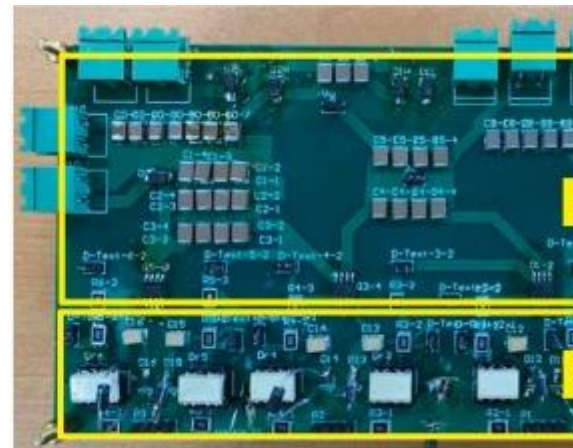
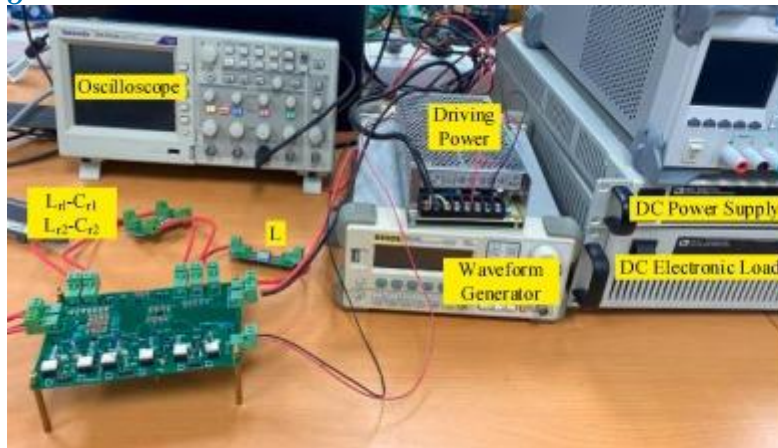


Fig. 15. Picture of the experimental test bench with the built 80 W prototype.  
Table 5. Components List.

Components	Value
$Q_1 - Q_6$	Dual MOSFET IRF7905, $R_{on}$ , 21.8 and 17.1m $\Omega$ for the upper and lower switches
Gate Driver	TLP250
$C_1 - C_5$	188 $\mu$ F Ceramic Capacitors
$C_{src}$	140 $\mu$ F Ceramic Capacitors
$C_{out}$	70 $\mu$ F Ceramic Capacitors
$C_{bat}$	110 $\mu$ F Ceramic Capacitors
$C_{r1}, C_{r2}$	2 $\mu$ F Ceramic Capacitors
$L_{r1}, L_{r2}$	0.47 $\mu$ H
$L$	33 $\mu$ H (on-resistance 30 m $\Omega$ at 100 kHz)
$D_H, D_L$	Schottky diode,

## 6.2. Experimental results for different modes

In order to verify different operation modes, main experimental results of the built SCI-TPC prototype during the battery charging mode and battery discharging mode were obtained and shown in Fig. 16(a) and Fig. 16(b), respectively. As shown in Fig. 16(a), during the battery charging mode, the measured node voltage  $V_x$  is a square wave, fluctuating between  $1/3in$  and  $2/3in$ , while  $V_y$  is a square wave with the fluctuation between  $2/3in$  and  $in$ . The measured resonant current  $i_{Lr}$  exhibits distinct four submodules: sinusoidal waveforms for submodule 1 and 3, while the corresponding waveforms within submodule 2 and 4 are zero. Besides, the measured current  $i_L$  was changing linearly. Specifically,  $i_L$  will be linearly increased for the submodule 1 and 2, while the corresponding current  $i_L$  for the submodule 3 and 4 will be linearly decreased.

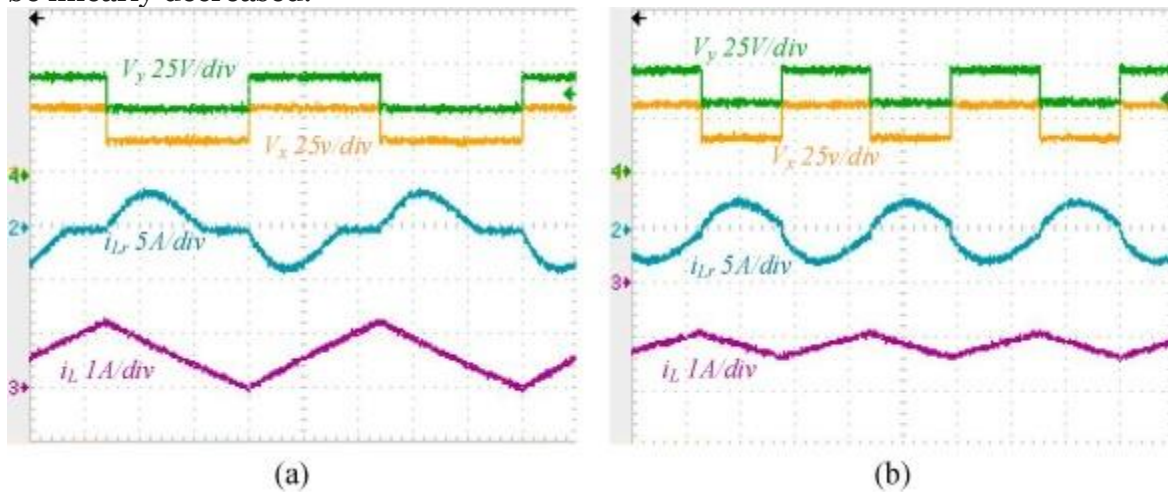


Fig. 16. Measured waveforms during different modes: (a) battery charging mode, (b) battery discharging mode.

## 6.3. Decoupling control evaluation

In order to analyze the interdependence between the bidirectional buck-boost converter and SRC of the SCI-TPC during the battery charging mode, the variations of  $V_{bat}$  and  $V_{out}$  were measured with respect to two control variables:  $F$  or  $d$ . Main

experimental results are shown in Fig. 17, which are consistent with the simulation results and the theoretical calculation results by equations (6), (12). According to Fig. 17, it can be concluded that  $V_{out}$  is dependent on  $F$  and independent of  $d$ , while  $V_{bat}$  is dependent on  $d$  and independent of  $F$ . Furthermore,  $V_{out}$  and  $V_{bat}$  can be well adjusted by the hybrid PWM/PFM algorithm.

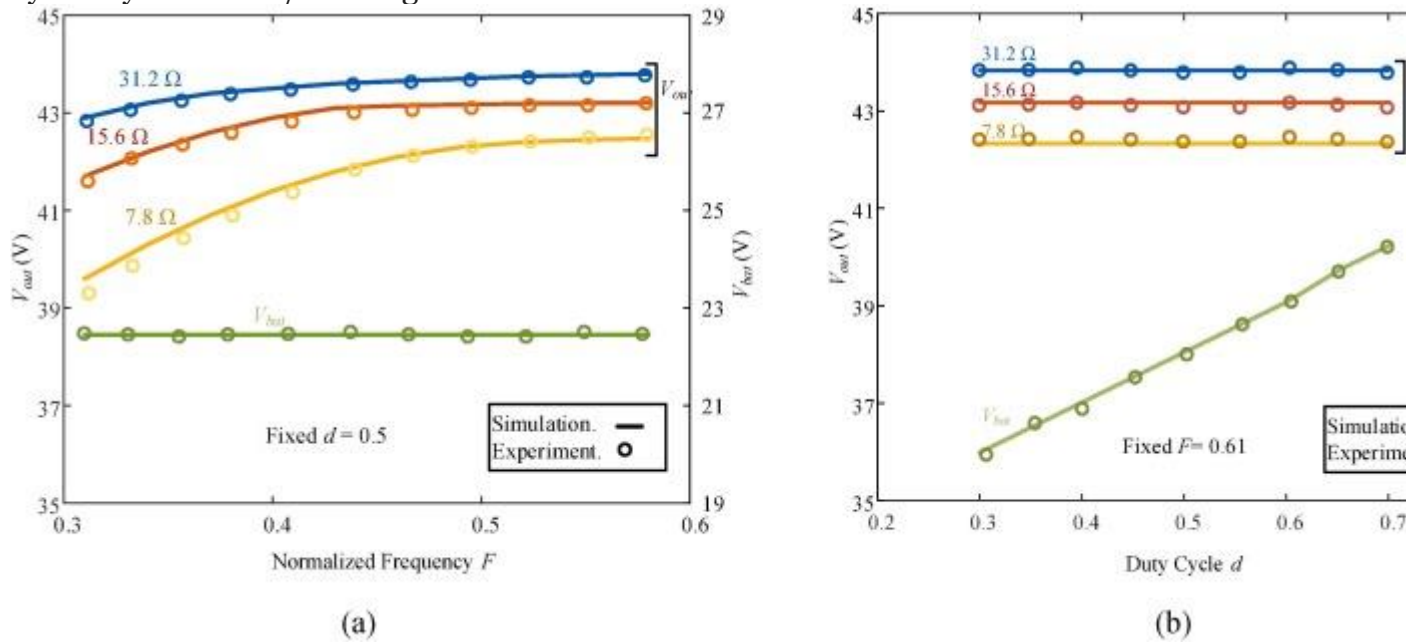


Fig. 17. Experimental characteristics of  $V_{out}$  and  $V_{bat}$  with respect to key control variables: (a) fixed  $d$ , and (b) fixed  $F$ .

Fig. 18 shows the experimental transient response under the changing conditions of  $I_{out}$  and  $I_{bat}$ . With the step change of  $I_{out}$ ,  $V_{bat}$  is not affected by the change of  $I_{out}$ , as shown in Fig. 18(a), which proves that  $V_{bat}$  controlled by PWM and  $V_{out}$  controlled by PFM can be decoupled and controlled independently. Similarly,  $V_{out}$  is not affected by the step change of  $I_{bat}$ , as shown in Fig. 18(b). These transient response results prove that the hybrid PWM/PFM can achieve a satisfactory control decoupling regulation performance for the SCI-TPC.

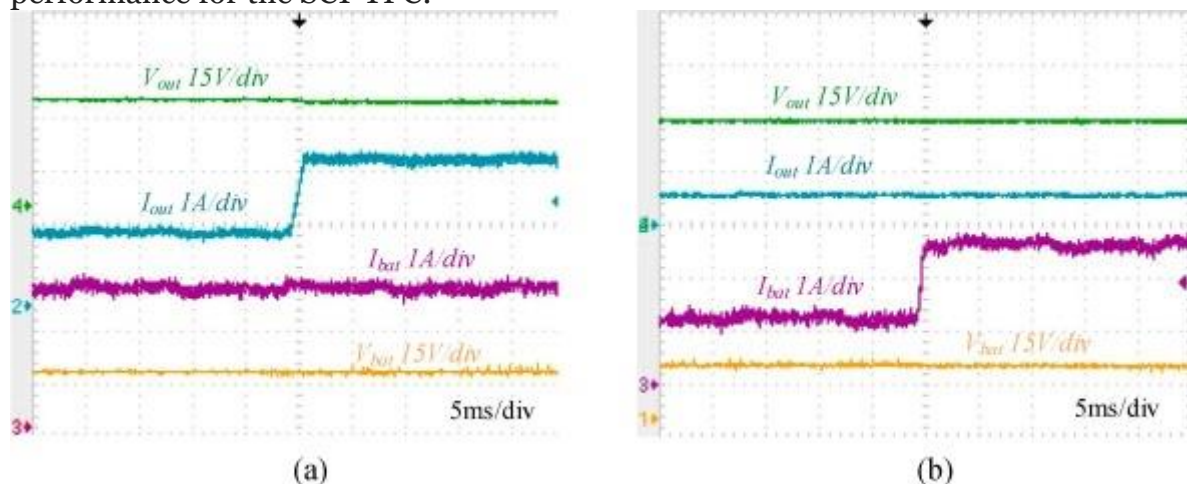


Fig. 18. Experimental transient response under different conditions: (a)  $I_{out}$  changed, and (b)  $I_{bat}$  changed.

#### 6.4. Power conversion efficiency

The power conversion efficiencies of the SCI-TPC during the battery charging mode and the battery discharging mode are defined as:(22)

where  $P_{out}$ ,  $P_{bat}$ , and  $P_{in}$  represent the load power, the battery charging or discharging power, and the input power, respectively.

The measured power conversion efficiencies during the battery charging mode at  $in=45$ ,  $out=43$  and  $bat=22$  are shown in Fig. 19(a), which indicates that the measured efficiency at a full load of  $out=60$  and  $bat=20$  is close to 95%. As shown in Fig. 19(a), with  $bat=0$ , the bidirectional buck-boost converter will not be involved and the measured efficiency is low especially for the light-load condition. However, with  $out=0$ , the SRC converter will not be involved and the measured system efficiency reaches about 94% at the beginning, as shown in Fig. 19(b). Thus, it can be concluded that the efficiency of SRC is not as high as that of the bidirectional buck-boost converter. Thus, with the increase of the output power,  $P_{out}$ , the measured efficiencies of the SCI-TPC is slightly decreased. Specifically, as shown in Fig. 19(a), with a fixed  $P_{bat}$ , the higher ratio of the SRC power involved in the total power, the lower efficiency will be observed. The measured power conversion efficiencies of the SCI-TPC during the battery discharging mode are shown in Fig. 19(c). With the optimized PWM/PFM hybrid modulation, the measured efficiency is found a few percent higher than that without optimization, which indicates that the optimized switching strategy based on equation is effective in improving the system efficiency.

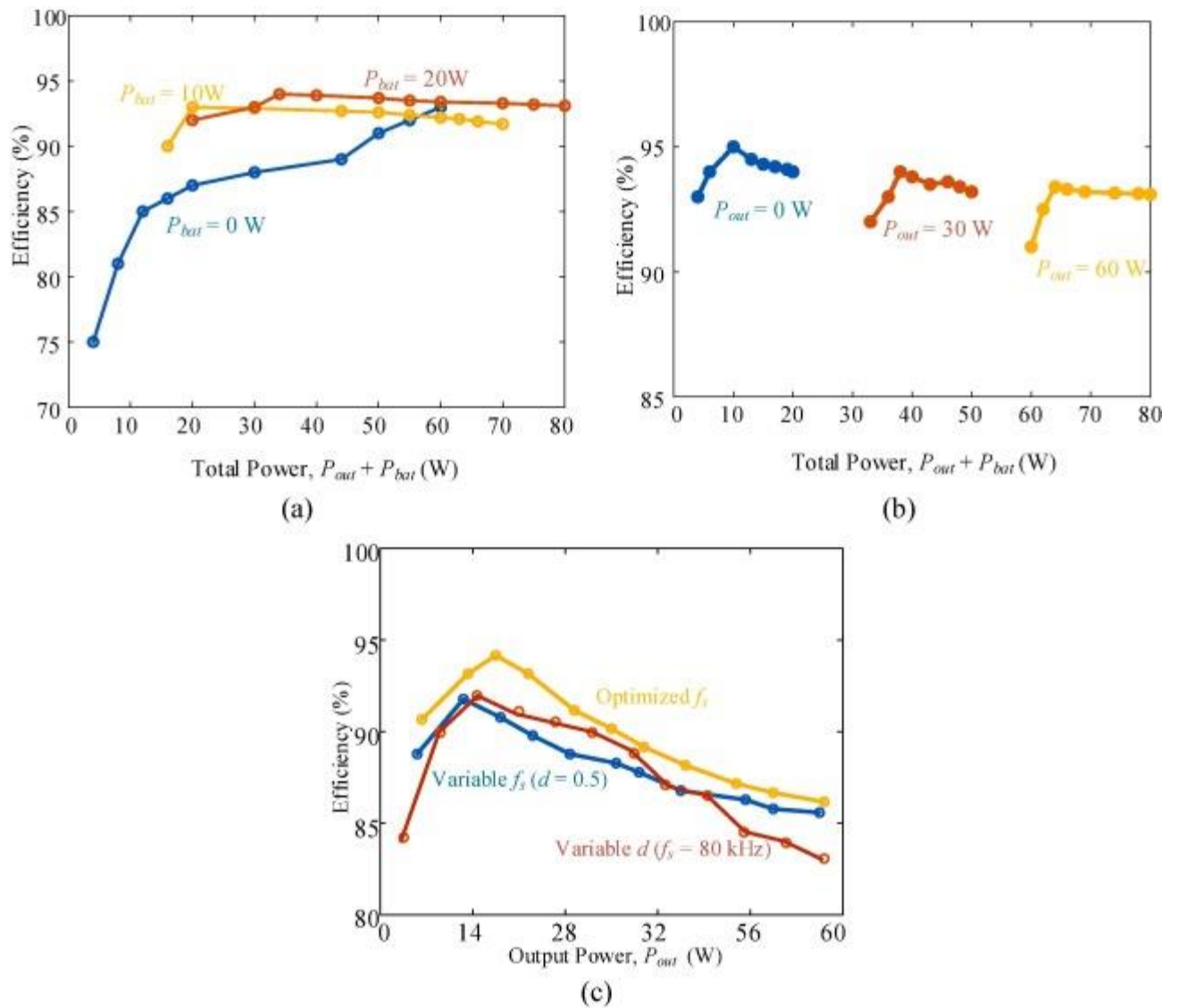


Fig. 19. Measured power conversion efficiencies during different modes: (a) the battery charging mode (fixed  $P_{bat}$ ), (b) the battery charging mode (fixed  $P_{out}$ ), and (c) the battery discharging mode.

During the battery charging mode, the measured efficiency of the SCI-TPC will change with respect to the switching frequency, as illustrated in Fig. 20. Three results indicate that when the switching frequency is equal to the resonant frequency, the  $I_{Lr\_RMS}$  is the smallest and the efficiency is the highest.

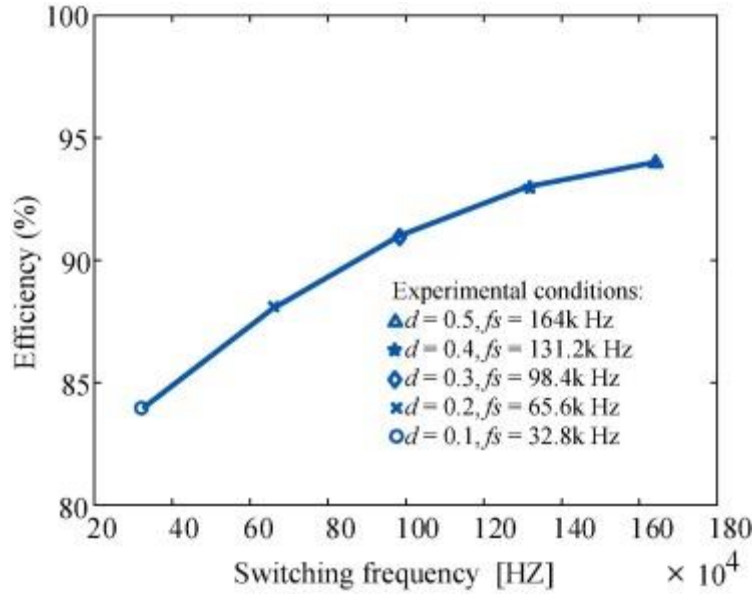


Fig. 20. Measured power conversion efficiencies with different switching frequencies.

### 6.5. Loss breakdown analysis

The loss breakdowns analysis of the SCI-TPC during the battery charging mode is illustrated in Fig. 21. It is obvious that the conduction loss of the schottky diode (DH, DL) and the switching losses of  $Q_5$  and  $Q_6$  located in the highest group account for a significant portion of the Joule loss. With a fixed  $P_{bat}$ , the total loss will increase rapidly with respect to  $P_{out}$ , as shown in Fig. 21(a). On the other hand, when  $P_{out}$  is fixed, the total loss increases with respect to  $P_{bat}$  will increase slowly, as shown in Fig. 21(b). The results indicate that SRC and SCC account for a major part of the total power loss Fig. 21. Loss breakdown analysis of the SCI-TPC during the battery charging mode; (a) at fixed  $P_{bat} = 20$  W, and (b) at fixed  $P_{out} = 60$  W.

## 7. Comparison

The SCI-TPC and MPC of the same power level are compared in terms of number of devices, control scheme, conversion ratio, inductor size, prototype volume, efficiency, and power density. The results are shown in Table 6. By comparison, it is found that SCI-TPC has great advantages in inductor miniaturization, converter volume reduction and power density increase due to the use of SCC structure. This will be very attractive for applications that require miniaturization of circuits, such as satellite power systems.

Table 6. Comparison of Main MPC Topologies.

Type	Component Count				Control Scheme	Conversion Ratio		Inductance	Volume	Light-Load Efficiency	Power Density
	Q	C	L	T		Battery Voltage Conversion Ratio	PV-Load Voltage Conversion Ratio				
FPI-TPC (Sato et al., 2020)	4	4	2	0	PWM/PS			High	Middle	Middle	0.5

Type	Component Count				Control Scheme	Conversion Ratio		Inductance	Volume	Light-Load Efficiency	Po
	Q	C	L	T		Battery Voltage Conversion Ratio	PV-Load Voltage Conversion Ratio				
MI-TPC (Uno et al., 2018)	2	4	0	1	PWM/PFM			Small	Large	Low	1.7
C-TPC (Nagata)	3	4	2	0	PWM			High	Middle	Middle	0.5
SCI-TPC	6	10	3	0	PWM/PFM			Low	Small	High	2.0

## 8. Conclusion

In this paper, a nonisolated switching-capacitor-integrated three-port converter (SCI-TPC) is presented by integrating a switching capacitor converter, a series resonant converter, and a bidirectional buck-boost converter to achieve single-stage direct power conversion among three ports: PV panels, batteries, and loads. With the SCI-TPC architecture, the square wave voltage generated on the switching node of the switching capacitor converter is used to drive the resonant tanks in SRC and the inductance in the bidirectional buck-boost converter, which can simplify the system structure, reduce the component count, and improve the operation reliability. A PWM/PFM hybrid control is adopted to realize the flexible power regulation for different operation modes and achieve power balance among three ports. During the battery charging mode, the output voltage and the battery voltage are regulated respectively so that the photovoltaic panel power generation can meet both the load power and the battery charging power. During the battery discharging mode, the output voltage is regulated so that the battery discharge power provides the output power separately. Moreover, the optimized PWM/PFM can reduce the current stress and improve the overall conversion efficiency over a full operating range. In order to validate the effectiveness of the optimized PWM/PFM for the SCI-TPC, an 80 W prototype was built and tested experimentally. The measured voltage conversion demonstrated that the output voltage and the battery voltage can be independently controlled by PFM and PWM without interference during the battery charging mode. Moreover, the measured efficiency of the prototype under a rated output power will be high up to 94%.

## Declaration of Competing Interest

The authors declare that they have no known competing financial interests or personal relationships that could have appeared to influence the work reported in this paper.

## Acknowledgements

This work was supported by the Research Development Fund of XJTU (RDF-16-01-10, RDF-17-01-28), the Research Enhancement Fund of XJTU (REF-17-01-02), the Suzhou Prospective Application Programme (SYG202016), and the XJTU Key Programme Special Fund (KSF-A-08, KSF-E-13, KSF-T-04).

## References

1. [Subudhi and Pradhan, 2013](#)  
B. Subudhi, R. Pradhan  
A Comparative Study on Maximum Power Point Tracking Techniques for Photovoltaic Power Systems  
IEEE Trans. Sustainable Energy, 4 (1) (2013), pp. 89-98
2. [Koutroulis et al., 2001](#)  
E. Koutroulis, K. Kalaitzakis, N.C. Voulgaris  
Development of a microcontroller-based, photovoltaic maximum power point tracking control system  
IEEE Trans. Power Electron., 16 (1) (2001), pp. 46-54
3. [Li et al., 2016](#)  
X. Li, H. Wen, L. Jiang, W. Xiao, Y. Du and C. Zhao. An Improved MPPT Method for PV System With Fast-Converging Speed and Zero Oscillation. IEEE Transactions on Industry Applications, vol. 52, no. 6, pp. 5051-5064, Nov.-Dec. 2016.
4. [Crăciun et al., 2014](#)  
B. Crăciun, T. Kerekes, D. Séra, R. Teodorescu  
Frequency Support Functions in Large PV Power Plants With Active Power Reserves  
IEEE Journal of Emerging and Selected Topics in Power Electronics, 2 (4) (2014), pp. 849-858
5. [Sangwongwanich et al., 2017](#)  
A. Sangwongwanich, Y. Yang, F. Blaabjerg  
A Sensorless Power Reserve Control Strategy for Two-Stage Grid-Connected PV Systems  
IEEE Trans. Power Electron., 32 (11) (2017), pp. 8559-8569



6. [Li et al., 2019](#)  
X. Li, H. Wen, Y. Zhu, L. Jiang, Y. Hu, W. Xiao  
A Novel Sensorless Photovoltaic Power Reserve Control With Simple Real-Time MPP Estimation  
IEEE Trans. Power Electron., 34 (8) (2019), pp. 7521-7531
7. [Zubair et al., 2015](#)  
R. Zubair, A. Ibrahim, M. Subhas  
Multi-input DC–D.C. converters in renewable energy applications - An overview  
Renew. Sustain. Energy Rev., 41 (2015), pp. 521-539
8. [Zhang et al., 2015](#)  
J. Zhang, H. Wu, X. Qin, Y. Xing  
PWM Plus Secondary-Side Phase-Shift Controlled Soft-Switching Full-Bridge Three-Port Converter for Renewable Power Systems  
IEEE Trans. Ind. Electron., 62 (11) (2015), pp. 7061-7072
9. [Liu et al., 2012](#)  
F. Liu, J. Ruan, X. Ruan  
A Systematic Approach to Synthesize Multi-port DC/DC Converters-Adopting Unipolar Pulsating Source Cells  
Proceedings of the CSEE, 32 (6) (2012), pp. 72-80
10. [Bhattacharjee et al., 2019](#)  
A.K. Bhattacharjee, N. Kutkut, I. Batarseh  
Review of Multiport Converters for Solar and Energy Storage Integration  
IEEE Trans. Power Electron., 34 (2) (2019), pp. 1431-1445
11. [Li et al., 2019](#)  
G. Li, J. Xia, K. Wang, Y. Deng, X. He, Y. Wang

Hybrid Modulation of Parallel-Series LLC Resonant Converter and Phase Shift Full-Bridge Converter for a Dual-Output DC–DC Converter

IEEE Journal of Emerging and Selected Topics in Power Electronics, 7 (2) (2019), pp. 833-842

12. [Hema Chander and Kumar, 2018](#)

A. Hema Chander, L. Kumar

MIC for reliable and efficient harvesting of solar energy

IET Power Electron., 12 (2) (2018), pp. 267-275

13. [Majeed et al., 2019](#)

Y.E. Majeed, I. Ahmad, D. Habibi

A multiple-input cascaded DC-DC converter for very small wind turbines

IEEE Trans. Ind. Electron., 66 (6) (2019), pp. 4414-4423

14. [Raghavendran et al., 2018](#)

S. Raghavendran, M. Umapathy, L.R. Karlmarx

Supercapacitor charging from piezoelectric energy harvesters using multi-input buck–boost converter

IET Circuits, Devices Syst., 12 (6) (2018), pp. 746-752

15. [Prabhala et al., 2016](#)

V.A.K. Prabhala, P. Fajri, V.S.P. Gouribhatla, B.P. Baddipadiga, M. Ferdowsi

A DC-DC Converter With High Voltage Gain and Two Input Boost Stages

IEEE Trans. Power Electron., 31 (6) (2016), pp. 4206-4215

16. [Zhao et al., 2015](#)

J. Zhao, H. H. C. Iu, T. Fernando, L. An, and D. Dah-Chuan Lu, “Design of a non-isolated single-switch three-port DC-DC converter for standalone PV-battery power system,” 2015 IEEE International Symposium on Circuits and Systems (ISCAS), May 2015, pp. 2493–2496.

17. [Honarjoo et al., 2018](#)

B. Honarjoo, S.M. Madani, M. Niroomand, E. Adib

Non-isolated high step-up three-port converter with single magnetic element for photovoltaic systems

IET Power Electron., 11 (13) (2018), pp. 2151-2160

18. [Mira et al., 2017](#)

M.C. Mira, Z. Zhang, A. Knott, M.A.E. Andersen

Analysis, Design, Modeling, and Control of an Interleaved-Boost Full-Bridge Three-Port Converter for Hybrid Renewable Energy Systems

IEEE Trans. Power Electron., 32 (2) (2017), pp. 1138-1155

19. [Zeng et al., 2019](#)

J. Zeng, Z. Yu, J. Liu, F. Liu

Triple-Compound-Full-Bridge- Based Multi-Input Converter (TCF-MIC) with Wide ZVS Range and Wide Conversion Gain

IEEE Trans. Ind. Electron. (2019)

20. [Buticchi et al., 2018](#)

G. Buticchi, L.F. Costa, D. Barater, M. Liserre, E.D. Amarillo

A Quadruple Active Bridge Converter for the Storage Integration on the More Electric Aircraft

IEEE Trans. Power Electron., 33 (9) (2018), pp. 8174-8186

21. [Lavanya et al., 2016](#)

A. Lavanya, J.D. Navamani, K. Vijayakumar, R. Rakesh

“Multi-input DC-DC converter topologies-a review”, international conference on electrical, electronics, and optimization techniques

ICEEOT, 2016 (2016), pp. 2230-2233

22. [Nielsen et al., 2012](#)

H.R. Nielsen, M.A.E. Andersen, Z. Zhang, O.C. Thomsen

Dual-input isolated full-bridge boost dc-dc converter based on the distributed transformers

IET Power Electron., 5 (7) (2012), pp. 1074-1083

23. [Zhang et al., 2012](#)

Z. Zhang, O.C. Thomsen, M.A.E. Andersen

Modeling and control of a dual-input isolated full-bridge boost converter

Proceedings of the Asia international model simulation conference (2012), pp. 2017-2023

24. [Zhigang and Fenlin, 2016](#)

G. Zhigang, J. Fenlin

Isolated multi-port DC-DC converter based on a high-frequency transformer

18th international conference on electrical machines and systems. ICEMS (2016), pp. 564-568

25. [Khosrogorji et al., 2016](#)

S. Khosrogorji, M. Ahmadian, H. Torkaman, S. Soori

Multi-input DC/DC converters in connection with distributed generation units - a review

Renew Sustain Energy Rev, 66 (2016), pp. 360-379

26. [Ding et al., 2013](#)

S. Ding, H. Wu, Y. Xing, Y. Fang, X. Ma

Topology and control of a family of non-isolated three-port dc-dc converters with a bidirectional cell

Proceedings of the IEEE applied power electron conference (2013), pp. 1089-1094

27. [Nahavandi et al., 2015](#)

A. Nahavandi, M. Tarafdar, M.B. Sharifian, S. Danyali

A non-isolated multi-input multi-output dc-dc boost converter for electric vehicle applications

IEEE Trans Power Electron, 30 (4) (2015), pp. 1818-1835

28. [Sanders et al., 2013](#)

S.R. Sanders, E. Alon, H.P. Le, M.D. Seeman, M. Jhon, V.W. Ng

The road to fully integrated dc-dc conversion via the switched-capacitor approach

IEEE Trans. Power Electron., 28 (9) (2013), pp. 4146-4155

29. [Lei et al., 2018](#)

Y. Lei, W.C. Liu, R.C.N.P. Podgurski

An analytical method to evaluate and design hybrid switched-capacitor and multilevel converters

IEEE Trans. Power Electron., 33 (3) (2018), pp. 2227-2240

30. [Midgley and Sigger, 1974](#)

D. Midgley, M. Sigger

Switched capacitors in power control

Proc. Inst. Elect, Eng., 121 (7) (1974), pp. 703-7043

31. [Oota et al., 1983](#)

I. Oota, T. Inoue, F. Ueno

A realization of low- power supplies using switched- capacitor transformers and its analysis

Trans, IECE, Japan., 66 (1983), pp. 576-583

32. [Sato et al., 2020](#)

Y. Sato, M. Uno, H. Nagata

Nonisolated Multiport Converters Based on Integration of PWM Converter and Phase-Shift-Switched Capacitor Converter

IEEE Trans. Power Electron., 35 (1) (2020), pp. 455-470

33. [Uno et al., 2018](#)

M. Uno, R. Oyama, K. Sugiyama

Partially Isolated Single-Magnetic Multiport Converter Based on Integration of Series-Resonant Converter and Bidirectional PWM Converter

IEEE Trans. Power Electron., 33 (11) (2018), pp. 9575-9587

34. [Nagata, xxxx](#)

H. Nagata and M. Uno, "Nonisolated PWM Three-Port Converter Realizing Reduced Circuit Volume for Satellite Electrical Power Systems," IEEE Transactions on Aerospace and Electronic Systems (Early Access).